nature nanotechnology

LETTERS

PUBLISHED ONLINE: 16 FEBRUARY 2015 | DOI: 10.1038/NNANO.2014.336

Microwave-driven coherent operation of a semiconductor quantum dot charge qubit

Dohun Kim[1], D. R. Ward[1], C. B. Simmons[1], John King Gamble[2], Robin Blume-Kohout[2], Erik Nielsen[2], D. E. Savage[3], M. G. Lagally[3], Mark Friesen[1], S. N. Coppersmith[1] and M. A. Eriksson[1]*

An intuitive realization of a qubit is an electron charge at two well-defined positions of a double quantum dot. This qubit is simple and has the potential for high-speed operation because of its strong coupling to electric fields. However, charge noise also couples strongly to this qubit, resulting in rapid dephasing at all but one special operating point called the 'sweet spot'. In previous studies d.c. voltage pulses have been used to manipulate semiconductor charge qubits[1–8] but did not achieve high-fidelity control, because d.c. gating requires excursions away from the sweet spot. Here, by using resonant a.c. microwave driving we achieve fast (greater than gigahertz) and universal single qubit rotations of a semiconductor charge qubit. The *Z*-axis rotations of the qubit are well protected at the sweet spot, and we demonstrate the same protection for rotations about arbitrary axes in the *X–Y* plane of the qubit Bloch sphere. We characterize the qubit operation using two tomographic approaches: standard process tomography[9,10] and gate set tomography[11]. Both methods consistently yield process fidelities greater than 86% with respect to a universal set of unitary single-qubit operations.

Coherent control of qubits with resonant microwaves plays an essential role in realizing precise single[10,12,13] and two[14] qubit gates in solid-state quantum computing architectures[15]. In electrically controlled quantum dots, driven coherent oscillations have been demonstrated in spin-based qubits using electron spin resonance[16–18], electric-dipole spin resonance[19–22] or resonant exchange gates[23], with typical rotation rates (Rabi frequencies) of <100 MHz. Here we demonstrate fast and coherent operation of a charge qubit in a double quantum dot in a silicon/silicon-germanium (Si/SiGe) heterostructure.

The charge qubit we study is formed by three electrons in a Si/SiGe double quantum dot (Fig. 1a)[7,24]. Figure 1c presents the qubit energy level diagram as a function of detuning with respect to the sweet spot, $\delta\varepsilon \equiv \varepsilon - \varepsilon_0$, where we define the sweet spot detuning ε_0 with $\partial E_{01}/\partial\varepsilon|_{\varepsilon_0} = 0$, where E_{01} is the difference in energy between the qubit states. Experimentally, the sweet spot is identified by finding the minimum resonant frequency in a microwave spectroscopy measurement performed as a function of detuning (see below). Detuning ε is controlled by gate GL or GR (Fig. 1a). States $|2,1\rangle = |L\rangle$ and $|1,2\rangle = |R\rangle$ (the ground states of the system at negative and positive ε, respectively) anticross near ε_0. A low-lying excited state outside the qubit space[25] and not visible in the energy range shown in the figure affects the dispersion of the energy levels shown and leads to non-zero ε_0, but is otherwise unimportant, because its occupation is negligible for the resonant driving demonstrated here.

Near the sweet spot ε_0, an avoided crossing is formed between states $|L\rangle$ and $|R\rangle$ with tunnel coupling strength Δ_1. The logical qubit states are the energy eigenstates at ε_0, which are approximately $|0\rangle \approx (|L\rangle + |R\rangle)/\sqrt{2}$ and $|1\rangle \approx (|L\rangle - |R\rangle)/\sqrt{2}$. As shown schematically by the black solid line in Fig. 1c, state $|L\rangle$ is first prepared by waiting longer than the charge relaxation time ($T_1 = 23.5$ ns) at a detuning appropriate for initialization and readout, $\delta\varepsilon_r \approx -160$ μeV (ref. 25). Ramping the gate voltage over a time of 4 ns changes the detuning to a value near $\delta\varepsilon = 0$, adiabatically evolving state $|L\rangle$ to state $|0\rangle$, completing the qubit initialization. A 10 ns microwave burst is then applied to gate GR. When the microwave frequency is resonant with the splitting between the qubit energy levels, excitation occurs from $|0\rangle$ to $|1\rangle$. The resulting probability of state $|1\rangle$, P_1, is measured by ramping the detuning adiabatically over ~2 ns back to $\delta\varepsilon_r$, which transforms $|0\rangle$ to $|L\rangle$ and $|1\rangle$ to $|R\rangle$, and measuring the change in I_{QPC} (ref. 25), where QPC indicates the quantum point contact. Details of the measurement procedure and conversion to probability are presented in Supplementary Section 1. By simulating the time evolution of the density matrix under the initialization and measurement ramp sequences, we estimate that the transformation of state $|L\rangle$ ($|R\rangle$) to state $|0\rangle$ ($|1\rangle$) is performed with a fidelity of over 99.99% (92%), with the lower fidelity for the transformation between $|R\rangle$ and $|1\rangle$ arising because of charge relaxation during the ramp (Supplementary Section 2). Figure 1b presents the resulting spectroscopy of the qubit energy levels. We find good agreement between the spectroscopic measurement and the calculated lowest-energy excitation spectrum (green dashed curve), with Hamiltonian parameters as measured in ref. 25. At the sweet spot $\partial E_{01}/\partial\varepsilon = 0$, the energy levels are first-order insensitive to detuning noise[5,7,23].

Coherent oscillations between qubit states $|0\rangle$ and $|1\rangle$ are implemented by applying the microwave sequence shown in Fig. 1c using an a.c. excitation frequency of $f_{ex} \approx 4.5$ GHz, which is resonant with the qubit at the sweet spot. Figure 1d shows the resulting microwave-driven Rabi oscillations in P_1, measured as a function of the microwave burst duration t_b and gate voltage V_{GL}, which determines the base level of $\delta\varepsilon$. Figure 1e shows periodic oscillations in P_1 at a frequency of $f_{Rabi} \approx 1$ GHz. The dependence of P_1 on t_b is well fit by an exponentially damped sine wave (Fig. 1e, red solid curve), with the best fit yielding a coherence time of $T_2^* = 1.5$ ns.

Figure 1f shows P_1 as a function of t_b and the peak-to-peak microwave amplitude V_{ac} (measured at the output of the waveform generator). The observed oscillation frequency varies linearly with V_{ac}, as expected for Rabi oscillations. Accounting for the filtering and attenuation in the dilution refrigerator, we estimate the peak-to-peak amplitude at the sample for $V_{ac} = 120$ mV to be 1.1 mV. These oscillations correspond to X-rotations of the qubit on the

[1]Department of Physics, University of Wisconsin-Madison, Madison, Wisconsin 53706, USA. [2]Sandia National Laboratories, Albuquerque, New Mexico 87185, USA. [3]Department of Materials Science and Engineering, University of Wisconsin-Madison, Madison, Wisconsin 53706, USA.
*e-mail: maeriksson@wisc.edu

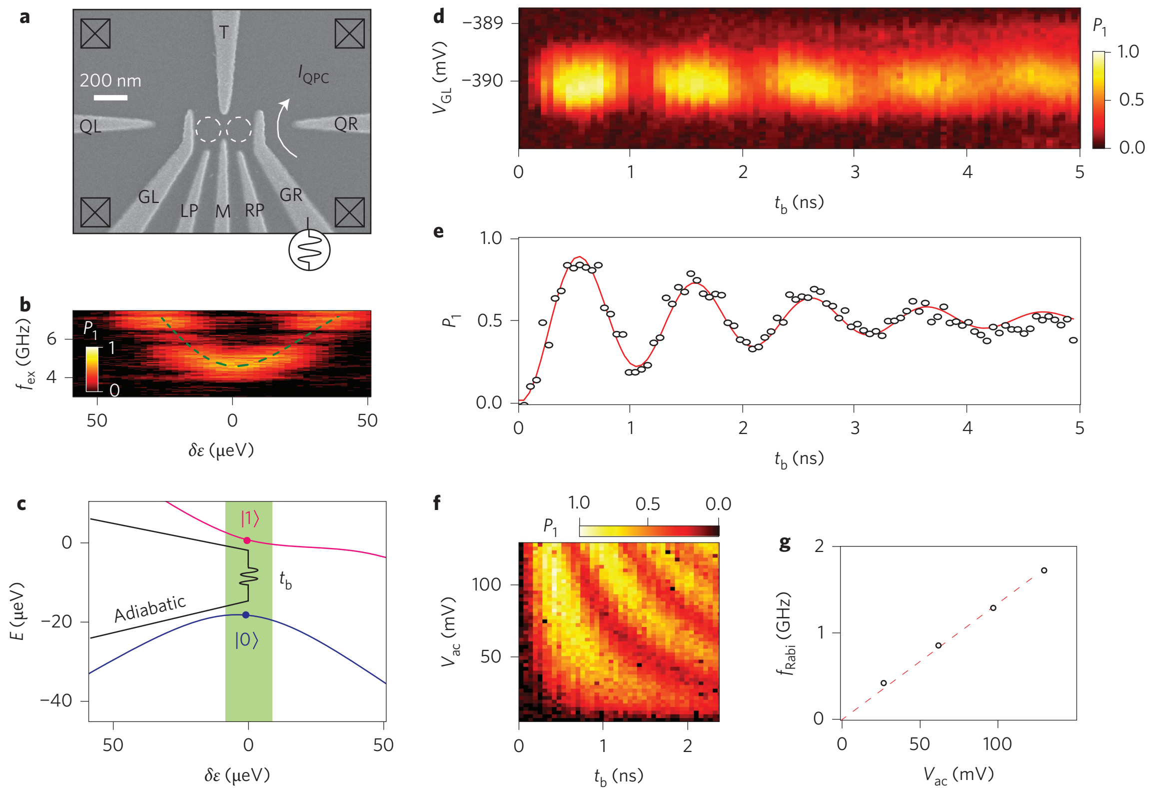

Figure 1 | Si/SiGe quantum dot device, qubit spectroscopy and coherent Rabi oscillation measurements. a, Scanning electron microscopy image of a device lithographically identical to the one used in the experiment[24]. **b**,**c**, Qubit energy levels and microwave spectroscopy. Probability P_1 (**b**) of the state to be $|1\rangle$ at the end of the driving sequence as a function of detuning change with respect to sweet spot $\delta\varepsilon$ and excitation frequency f_{ex} of the microwaves applied to gate GR. The dashed green curve shows a fit to the calculated energy difference between the ground state and the lowest-energy excited state of the four-level model of ref. 25 (see also Supplementary Section 2). Diagram of the calculated energy levels E versus $\delta\varepsilon$ (**c**), including the ground states of the (2,1) and (1,2) charge configurations, $|L\rangle$ and $|R\rangle$, respectively, and logical states $|0\rangle \approx (|L\rangle + |R\rangle)/\sqrt{2}$ and $|1\rangle \approx (|L\rangle - |R\rangle)/\sqrt{2}$. Black solid line inset in **c**: pulse sequence used for Rabi oscillation and spectroscopy measurements. The green shaded region indicates the detuning energy at which microwave pulses are applied. **d**,**e**, Rabi oscillations. P_1 as a function of voltage V_{GL} and microwave pulse duration t_b (**d**) with f_{ex} = 4.54 GHz and excitation amplitude V_{ac} = 70 mV. Line-cut of P_1 near V_{GL} = –390 mV (**e**), showing ~1 GHz coherent Rabi oscillations. Red solid curve shows a fit to an exponentially damped sine wave with best fit parameter T_2^* = 1.5 ns. **f**,**g**, Dependence of the Rabi oscillation frequency on microwave amplitude. P_1 as a function of V_{ac} and t_b (**f**) with f_{ex} = 4.54 GHz. Rabi oscillation frequency f_{Rabi} as a function of V_{ac} (**g**) with fixed f_{ex} = 4.54 GHz, showing good agreement of a linear fit (red dashed line) to the data.

Bloch sphere, and for the fastest rotations observed an $X_{\pi/2}$ gate has a duration of 125 ps.

We now demonstrate Z-axis rotations of the qubit by performing a Ramsey fringe experiment using the microwave pulse sequence shown schematically in Fig. 2a. We first prepare the state $|Y\rangle = \sqrt{(1/2)}(|0\rangle + i|1\rangle)$ by initializing to $|L\rangle$, adiabatically changing the detuning to $\delta\varepsilon = 0$ to evolve the state to $|0\rangle$, and then performing an $X_{\pi/2}$ rotation at this detuning. Z-axis rotation results from the evolution of a relative phase between states $|0\rangle$ and $|1\rangle$, given by $\varphi = -t_e 2\Delta_1/\hbar$, where t_e is the time spent at $\delta\varepsilon = 0$. The resulting state is rotated by a second $X_{\pi/2}$ microwave pulse, and the final probability P_1 again is measured by adiabatically projecting state $|1\rangle$ to $|R\rangle$ at the readout position $\delta\varepsilon_r$. Figure 2b,c shows the resulting Ramsey fringes, which are quantum oscillations of the qubit state around the Z-axis of the Bloch sphere. By fitting the oscillations to an exponentially damped sine wave (red solid curve), we extract a dephasing time $T_2^* = 1.3$ ns and an oscillation frequency of 4.5 GHz, the latter being consistent with the spectroscopic measurements shown in Fig. 1b. The observed T_2^* times are on the order of nanoseconds both for X (Rabi) and Z (Ramsey) rotations, which is an important improvement arising from the a.c. gating and the ability to perform a universal set of single qubit operations at the sweet spot. Data in Supplementary Section 3 show that T_2^* is much shorter (on the order of 100 ps) away from the sweet spot.

Using a.c. gating we can choose the rotation axis to point in an arbitrary direction in the X–Y plane of the Bloch sphere by controlling the phase of the applied microwave burst. On resonance in the rotating frame, the Hamilton takes the form $H = \cos(\phi)\sigma_x + \sin(\phi)\sigma_y$, where σ_i are Pauli matrices and ϕ is the relative phase of the microwave burst with respect to the first pulse incident on the qubit[26]. Controlling ϕ thus enables rotations of the qubit around any axis lying in the X–Y plane of the Bloch sphere. Figure 2d presents the measurement of P_1 using such a pulse sequence as a function of both ϕ and t_e, demonstrating a smooth variation in P_1 arising from changes in the control parameters. Figure 2e shows line-cuts of P_1 at $\phi = 0$, 90° and 180° (corresponding to the second pulse inducing a $\pi/2$ rotation around the X, Y and $-X$ axes, respectively); microwave phase control clearly enables control of the phase of the resulting Ramsey fringes. Taken together, the data summarized in Figs 1 and 2 demonstrate control of the qubit over the entire Bloch sphere.

We characterized decoherence times by implementing a Hahn echo[17,27,28] of the a.c.-gated charge qubit by applying the pulse sequence shown in Fig. 3a. Inserting an X_π pulse between state initialization and measurement corrects for noise that is static on the timescale of the pulse sequence. In Fig. 3b,c, while keeping the total free evolution time τ fixed, we sweep the position of the decoupling X_π pulse to reveal an echo envelope[7,28]. The maximum amplitude of the observed envelope reveals the extent to which the

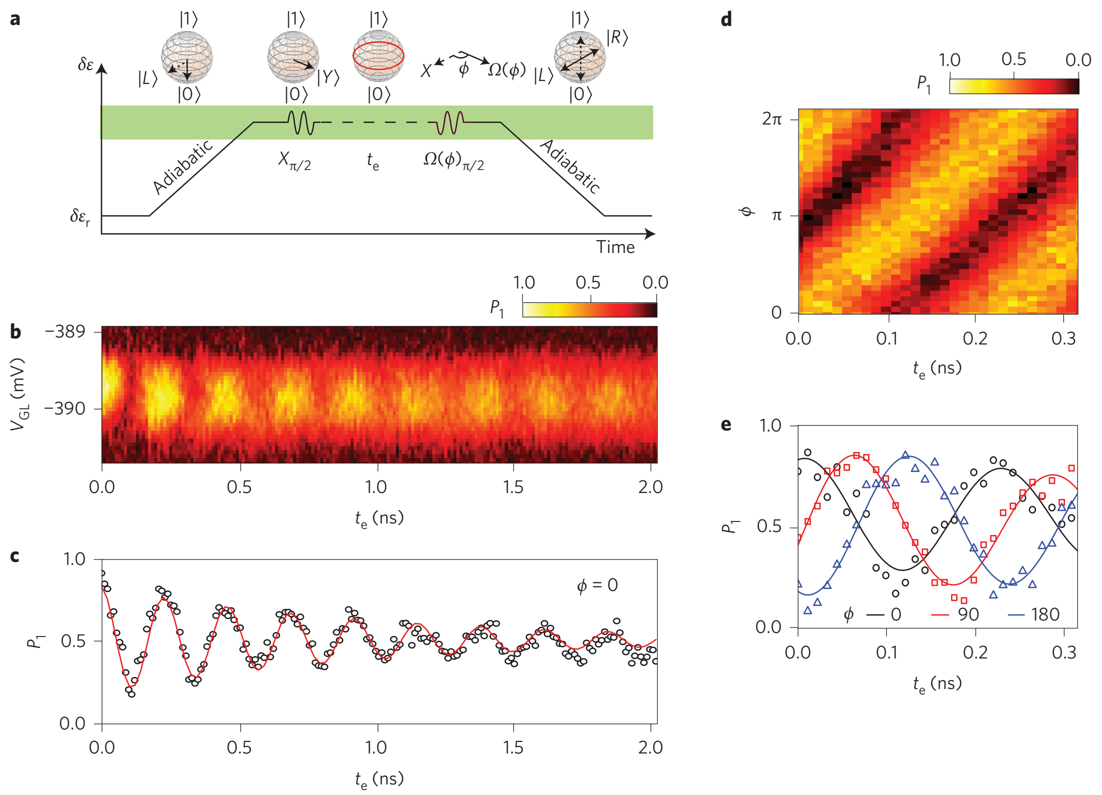

Figure 2 | Ramsey fringes and demonstration of three-axis control of the a.c.-gated charge qubit. a, Schematic of the pulse sequences used to perform universal control of the qubit. Both the delay t_e and phase ϕ of the second microwave pulse are varied in the experiment. The green shading corresponds to the part of the pulse sequence that occurs at detunings shaded green in Fig. 1c. **b**,**c**, Experimental measurement of Z-axis rotation. The first $X_{\pi/2}$ gate rotates the Bloch vector onto the X-Y plane, and the second $X_{\pi/2}$ gate ($\phi = 0$) is delayed with respect to the first gate by t_e, during which time the state evolves freely around the Z-axis of the Bloch sphere. P_1 as a function of V_{GL} and t_e (**b**) for states initialized near $|Y\rangle$. Line-cut of P_1 near V_{GL} = –390 mV (**c**), showing ~4.5 GHz Ramsey fringes. The red solid curve shows a fit to an exponentially damped sine wave with best fit parameter T_2^* = 1.3 ns. **d**,**e**, Control of qubit rotations about an arbitrary axis in the X-Y plane. P_1 as a function of ϕ and t_e (**d**). Line-cut of **d** at $\phi = 0$ (X-axis, black), 90° (Y-axis, red) and 180°(–X-axis, blue) (**e**). The coherent Z-axis rotation along with the rotation axis control with ϕ demonstrates full control of the qubit states around three orthogonal axes on the Bloch sphere.

state has dephased during the free evolution time τ, characterized by $T_{2,\text{echo}}$, whereas the amplitude decays as a function of δt with inhomogeneous decay time T_2^*. The oscillations of P_1 in Fig. 3b,c are observed as a function of δt at twice the Ramsey frequency ($2f_{\text{Ramsey}} \approx 9$ GHz) and are well fit by a Gaussian decay (red solid curve). Figure 3d shows the echo amplitude decay as a function of τ; for each τ the echo amplitude is determined by fitting the echo envelope to a Gaussian decay similar to Fig. 3c, yielding the dephasing time $T_{2,\text{echo}} \approx 2.2 \pm 0.1$ ns. Although further work is needed to better understand the decoherence mechanisms of semiconductor charge qubits, the coherence time demonstrated here is most likely limited by charge noise in the system, because piezoelectric phonons are absent in Si. We note that the charge relaxation time falls below ~10 ns near the sweet spot (Supplementary Section 2), which also may affect the overall coherence time in the current experiment.

The ultimate test of experimental qubit control is the demonstration of repeatable quantum logic gates. Although the $\pi/2$ rotations that generate the Clifford group are commonly demonstrated, a.c. control allows direct implementation of any unitary. We therefore validated two distinct gate sets: (1) high-fidelity approximations to $\{X_{\pi/2}, Z_{\pi/2}\}$ and (2) a set of three arbitrarily chosen near-unitary operations $\{G_1, G_2, G_3\}$. We used standard quantum process tomography (QPT)[9,10] to characterize the first gate set. Figure 4a shows the resulting process matrices (χ) expressed in the Pauli basis: solid bars represent the ideal 'target' quantum processes, and open circles show the results of QPT. The process fidelities[29] between the QPT estimates and the targets are $F = 86\%$ and $F = 91\%$ for the $X_{\pi/2}$ and $Z_{\pi/2}$ operations, respectively. QPT relies on prior knowledge of input states and final measurements that are implemented using the same logic gates that we seek to characterize. Therefore, we also applied a technique called gate set tomography (GST)[11], which avoids these assumptions. GST characterizes logic gates and state preparation/measurement simultaneously and self-consistently, by representing all of them as unknown process matrices. Because this frees us from any obligation to use carefully calibrated operations, we applied GST to the set of three repeatable but uncalibrated logic gates we denote $\{G_1, G_2, G_3\}$.

Data for GST are obtained from many repetitions of several specific experiments, each described by a specific sequence of operations: (1) initialize the qubit in state ρ; (2) perform a sequence of $L \in [0 \ldots 32]$ operations chosen from $\{G_1, G_2, G_3\}$; (3) perform measurement M. Statistical analysis (a variant of maximum likelihood estimation) is used to find the estimates $\{\hat{G}_1, \hat{G}_2, \hat{G}_3, \rho, \mathcal{M}\}$ that are most consistent with the measurements (see Supplementary Section 4 for more details). Because we did not set out to implement any particular rotations, we compute *ex post facto* the closest unitary rotations to these estimates and define these as the 'target' gates. The results are shown in Fig. 4b,c. Figure 4b shows the elements of the process (χ) matrix for the GST estimates (triangles) and the closest-unitary 'targets' (solid bars). Figure 4c portrays those unitaries as rotations on the Bloch sphere.

We also performed QPT on the G_1 and G_3 gates to confirm and validate the GST results. QPT depends critically on known gates, so

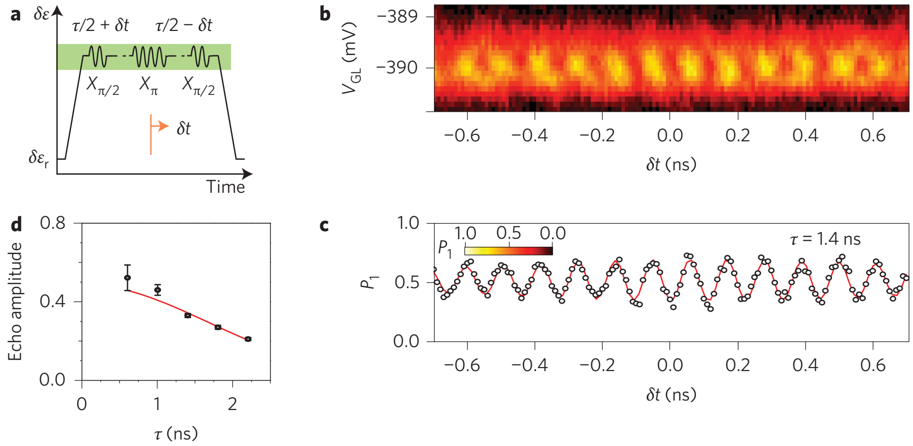

Figure 3 | Hahn echo measurement. **a**, Schematic pulse sequence for the measurement of Hahn echo that corrects for noise that is static on the timescale of the pulse sequence[17,27,28]. The green shading corresponds to the part of the pulse sequence that occurs at detunings shaded green in Fig. 1c. **b**,**c**, Typical echo measurements with fixed total evolution time $\tau = 1.4$ ns. P_1 as a function of V_{GL} and delay time δt of the X_{π} pulse (**b**). The effects of static inhomogeneities are minimized at $\delta t = 0$, and oscillations of P_1 as function of δt at twice the Ramsey frequency decay with δt at the inhomogeneous decay rate $1/T_2^*$. The magnitude of the signal at $\delta t = 0$ as the wait time τ is varied decays at the homogeneous decay rate $1/T_{2,\mathrm{echo}}$. Line-cut of P_1 near $V_{GL} = -390$ mV (**c**) showing oscillations at twice the Ramsey frequency, ~9 GHz. The solid red curve is a fit to a Gaussian envelope with fixed $T_2^* = 1.3$ ns assessed by Ramsey fringe measurement. **d**, Echo amplitude as a function of τ. The amplitude is determined by fitting data like that shown in **c** to a sine wave with a Gaussian decay, and the error bars are the uncertainty in that fit. The solid red curve is a Gaussian fit with $T_{2,\mathrm{echo}} = 2.2 \pm 0.1$ ns. Applying the Hahn echo sequence increases the dephasing time, indicating that a significant component of the dephasing arises from low-frequency noise processes.

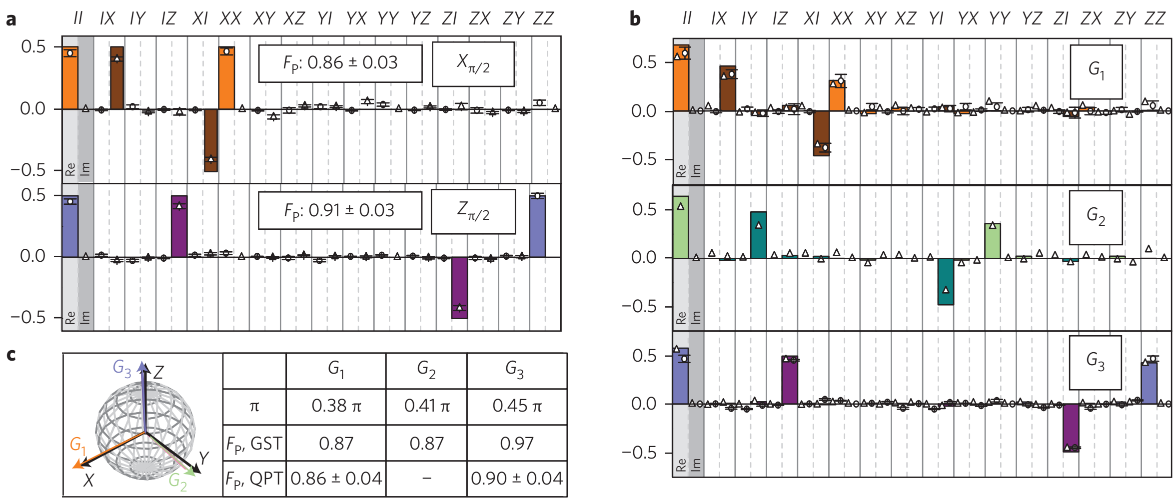

Figure 4 | QPT and GST of the a.c.-gated charge qubit. **a**, Real and imaginary parts of the elements of the process matrix χ (ref. 9) in the Pauli basis $\{I, X, Y, Z\}$ for $X_{\pi/2}$ and $Z_{\pi/2}$ processes: ideal 'targets' (solid bars), and standard QPT estimates (open circles, real part; open triangles, imaginary part). **b**, χ for uncalibrated operations G_1, G_2 and G_3, obtained by GST[11] (triangles) and standard QPT[9,10,25] (open circles), compared to target gates T_1, T_2 and T_3 (solid bars). Because these gates are not precalibrated, the target gates are defined to be the unitary processes closest to the GST estimates of G_1, G_2 and G_3 in the Frobenius norm. GST self-consistently determines the state preparation, gate operations and measurement processes[11]. **c**, Rotation axes on the Bloch sphere, rotation angle θ and process fidelities obtained by GST (F_p, GST) and QPT (F_p, QPT) for three processes G_1, G_2 and G_3. Here, the rotation axis and angle correspond to the closest unitary operations to the GST estimate (T_1, T_2 and T_3); the process fidelities are also taken between the estimates and these target processes. The error on F_p, QPT was estimated by repeating QPT using ten distinct sets of input and output states; standard deviations are reported. GST and QPT yield consistent results, with process fidelities of ≥86% for all gates.

we used the GST closest-unitary approximations for G_1 and G_3 to model the preparation of input states and final measurements for QPT. To distil a single figure of merit, we computed the process fidelity F between our estimates (both GST and QPT) and the closest unitary rotation. Its interpretation is slightly different in this context; because the targets were computed *ex post facto*, $1-F$ quantifies the amount of incoherent error in our gate implementation, whereas with a pre-existing target, it also quantifies coherent under/over-rotation errors. These process fidelities, shown for both GST and QPT in Fig. 4c, are consistent both with each other and with the process fidelities calculated in Fig. 4a.

Coherent microwave a.c.-gating of a semiconductor quantum dot charge qubit offers fast (greater than gigahertz) manipulation rates for all elementary rotation axes. Because all gates can be performed at the sweet spot where the decoherence time is >1 ns instead of ~100 ps (refs 6,7), rotations around three orthogonal axes of the Bloch sphere with process fidelities higher than 86% are achieved. This improvement is analogous to early developments in superconducting charge qubits[4,12], where operating at a sweet spot with resonant microwaves[12] demonstrated the first high-quality universal single qubit gate operations after the initial demonstration of charge qubit manipulation with non-adiabatic pulse techniques[4]. Applying a Hahn-echo decoupling sequence provides modest improvement in the coherence time ($T_{2,\mathrm{echo}} \approx 2.2$ ns compared to $T_2^{\star} \approx 1.3$ ns), indicating that understanding high-frequency charge noise as well as charge relaxation at the sweet spot will be important for further development. The quantum dot charge qubit is highly tunable using gate voltages, and we expect that investigating coherence and process fidelity as a function of tunnel coupling strength between the dots will provide an effective route to improve its performance[5].

Methods

Measurements. The experiments were performed on a double quantum dot fabricated in a Si/SiGe heterostructure[7,30] at base temperature (electron temperature of ~140 mK; ref. 30) in a dilution refrigerator. The valence electron occupation of the double dot was (2,1) or (1,2), as confirmed by magnetospectroscopy measurements[30]. All manipulation sequences including microwave bursts were generated by a Tektronix 70002A arbitrary waveform generator and were added to the dot-defining d.c. voltage through a bias-tee (Picosecond Pulselabs 5546-107) before being applied to gate GR. Similarly to our previous study[25], the conductance change through the QPC with and without the applied microwave burst, and measured with a lock-in amplifier (EG&G model 7265), was used to determine the average charge occupation and was converted to the reported probabilities. Charge relaxation during the measurement phase was taken into account using the measured charge relaxation time of $T_1 \approx 23.5$ ns at the readout detuning of $\delta\varepsilon_r \approx -160$ μeV (ref. 25). Supplementary Section 1 presents details of the measurement technique and the probability normalization.

GST. GST was performed in two stages, as described in ref. 11. First, a rough estimate was obtained by analysing data from short gate sequences using linear inversion. Next, data from long sequences were incorporated using maximum-likelihood parameter estimation to refine the preliminary estimate. The required gate sequences were defined using a set of fiducial sequences $\mathcal{F} = \{F_i\}$ that fix a consistent (but *a priori* unknown) reference frame. Here, we chose $\mathcal{F} = \{\varnothing, G_1, G_2, G_1^3\}$, where $\varnothing$ is the null operation (do nothing for no time). In terms of these fiducials, linear inversion GST demands data from all sequences of the form $F_i G_k F_j$, where $i,j = 1\ldots4$ and $k = 0\ldots3$ and $G_0 \equiv \varnothing$ is the null operation. Supplementary Section 4 provides more details about the GST implemented here.

Received 2 July 2014; accepted 18 December 2014; published online 16 February 2015

References

1. Cao, G. *et al.* Ultrafast universal quantum control of a quantum-dot charge qubit using Landau–Zener–Stückelberg interference. *Nature Commun.* **4,** 1401 (2013).
2. Shinkai, G., Hayashi, T., Ota, T. & Fujisawa, T. Correlated coherent oscillations in coupled semiconductor charge qubits. *Phys. Rev. Lett.* **103,** 056802 (2009).
3. Hayashi, T., Fujisawa, T., Cheong, H. D., Jeong, Y. H. & Hirayama, Y. Coherent manipulation of electronic states in a double quantum dot. *Phys. Rev. Lett.* **91,** 226804 (2003).
4. Nakamura, Y., Pashkin, Y. A. & Tsai, J. S. Coherent control of macroscopic quantum states in a single-Cooper-pair box. *Nature* **398,** 786–788 (1999).
5. Petersson, K. D., Petta, J. R., Lu, H. & Gossard, A. C. Quantum coherence in a one-electron semiconductor charge qubit. *Phys. Rev. Lett.* **105,** 246804 (2010).
6. Dovzhenko, Y. *et al.* Nonadiabatic quantum control of a semiconductor charge qubit. *Phys. Rev. B* **84,** 161302 (2011).
7. Shi, Z. *et al.* Coherent quantum oscillations and echo measurements of a Si charge qubit. *Phys. Rev. B* **88,** 075416 (2013).
8. Gorman, J., Hasko, D. G. & Williams, D. A. Charge-qubit operation of an isolated double quantum dot. *Phys. Rev. Lett.* **95,** 090502 (2005).
9. Nielsen, M. A. & Chuang, I. L. *Quantum Computation and Quantum Information* (Cambridge Univ. Press, 2000).
10. Chow, J. M. *et al.* Randomized benchmarking and process tomography for gate errors in a solid-state qubit. *Phys. Rev. Lett.* **102,** 090502 (2009).
11. Blume-Kohout, R. *et al.* (2013). Robust, self-consistent closed-form tomography of quantum logic gates on a trapped ion qubit. Preprint http://arxiv.org/abs/1310.4492.
12. Vion, D. *et al.* Manipulating the quantum state of an electrical circuit. *Science* **296,** 886–889 (2002).
13. Chow, J. M. *et al.* Optimized driving of superconducting artificial atoms for improved single-qubit gates. *Phys. Rev. A* **82,** 040305 (2010).
14. Fedorov, A., Steffen, L., Baur, M., da Silva, M. P. & Wallraff, A. Implementation of a Toffoli gate with superconducting circuits. *Nature* **481,** 170–172 (2012).
15. DiVincenzo, D. P. The physical implementation of quantum computation. *Fortschr. Phys.* **48,** 771–783 (2000).
16. Koppens, F. H. L. *et al.* Driven coherent oscillations of a single electron spin in a quantum dot. *Nature* **442,** 766–771 (2006).
17. Koppens, F. H. L., Nowack, K. C. & Vandersypen, L. M. K. Spin echo of a single electron spin in a quantum dot. *Phys. Rev. Lett.* **100,** 236802 (2008).
18. Pla, J. J. *et al.* A single-atom electron spin qubit in silicon. *Nature* **489,** 541–545 (2012).
19. Nowack, K. C., Koppens, F. H. L., Nazarov, Y. V. & Vandersypen, L. M. K. Coherent control of a single electron spin with electric fields. *Science* **318,** 1430–1433 (2007).
20. van den Berg, J. W. G. *et al.* Fast spin–orbit qubit in an indium antimonide nanowire. *Phys. Rev. Lett.* **110,** 066806 (2013).
21. Petersson, K. D. *et al.* Circuit quantum electrodynamics with a spin qubit. *Nature* **490,** 380–383 (2012).
22. Kawakami, E. *et al.* Electrical control of a long-lived spin qubit in a Si/SiGe quantum dot. *Nature Nanotech.* **9,** 666–670 (2014).
23. Medford, J. *et al.* Quantum-dot-based resonant exchange qubit. *Phys. Rev. Lett.* **111,** 050501 (2013).
24. Shi, Z. *et al.* Fast coherent manipulation of three-electron states in a double quantum dot. *Nature Commun.* **5,** 3020 (2014).
25. Kim, D. *et al.* Quantum control and process tomography of a semiconductor quantum dot hybrid qubit. *Nature* **511,** 70–74 (2014).
26. Shore, B. W. *The Theory of Coherent Atomic Excitation* (Wiley, 1990).
27. Vandersypen, L. M. K. & Chuang, I. L. NMR techniques for quantum control and computation. *Rev. Mod. Phys.* **76,** 1037–1069 (2005).
28. Dial, O. E. *et al.* Charge noise spectroscopy using coherent exchange oscillations in a singlet–triplet qubit. *Phys. Rev. Lett.* **110,** 146804 (2013).
29. Magesan, E., Blume-Kohout, R. & Emerson, J. Gate fidelity fluctuations and quantum process invariants. *Phys. Rev. A* **84,** 012309 (2011).
30. Simmons, C. B. *et al.* Tunable spin loading and T_1 of a silicon spin qubit measured by single-shot readout. *Phys. Rev. Lett.* **106,** 156804 (2011).

Acknowledgements

This work was supported in part by the Army Research Office (W911NF-12-0607), the National Science Foundation (PHY-1104660) and by the Laboratory Directed Research and Development programme at Sandia National Laboratories. Sandia National Laboratories is a multi-programme laboratory managed and operated by Sandia Corporation, a wholly owned subsidiary of Lockheed Martin Corporation, for the United States Department of Energy's National Nuclear Security Administration (contract DE-AC04-94AL85000). Development and maintenance of the growth facilities used for fabricating samples is supported by the Department of Energy (DE-FG02-03ER46028). This research utilized National Science Foundation-supported shared facilities at the University of Wisconsin–Madison.

Author contributions

D.K. performed electrical measurements, state and process tomography, and analysed the data with M.A.E., M.F. and S.N.C. D.R.W. developed the hardware and software for measurements. C.B.S. fabricated the quantum dot device. J.K.G., R.B-K. and E.N. performed gate-set tomography. D.E.S. and M.G.L. prepared the Si/SiGe heterostructure. All authors contributed to the preparation of the manuscript.

Additional information

Supplementary information is available in the online version of the paper. Reprints and permissions information is available online at www.nature.com/reprints. Correspondence and requests for materials should be addressed to M.A.E.

Competing financial interests

The authors declare no competing financial interests.